Properties of the RFI Environment at 1400–1427 MHz as Observed by the Soil Moisture Active/Passive Mission Microwave Radiometer

A. Bringer, *Member, IEEE*, J. T. Johnson, *Fellow, IEEE*, Y. Soldo, *Member, IEEE*, D. M. Le Vine, *Fellow, IEEE*, P. Mohammed, *Member, IEEE*, S. Misra, *Senior Member, IEEE*, P. de Matthaeis, *Senior Member, IEEE*, and J. R. Piepmeier, *Senior Member, IEEE*

***Abstract*—The soil moisture active/passive (SMAP) satellite microwave radiometer has been providing global measurements of L-band thermal emission from Earth since April 2015. Although the radiometer operates in the protected 1400–1427 MHz portion of the radio spectrum, its measurements are still corrupted by either radio frequency interference (RFI) from out-of-band emissions via legal sources or by sources operating in-band illegally. The SMAP radiometer includes a digital backend that enables implementation of multiple ground-based RFI detection and filtering algorithms. This data is used to collect statistics and trends of Earth's RFI environment. This article examines properties of the global RFI environment as observed by SMAP, including information on RFI source properties (obtained from analysis of SMAP multiple detector outputs) and the evolution of the RFI environment in time. Residual RFI contributions after the application of SMAP RFI processing are also examined as preliminary information for the development of future methods to address their effect.**

***Index Terms*—L-band radiometry, radio frequency interference (RFI), RFI detection, SMAP.**

Introduction

MEASUREMENTS of Earth's natural thermal emissions in the protected 1400–1427 MHz portion of the radio spectrum can be used to monitor soil moisture, ocean salinity, and other Earth surface properties, as demonstrated by the soil moisture ocean salinity (SMOS) [1], Aquarius [2], and soil moisture active and passive (SMAP) [3] missions. Despite the use of a protected portion of the spectrum, all of these missions have reported significant corruption of their measurements by radio frequency interference (RFI) caused either by out-of-band emissions from sources near this portion of the spectrum or by transmitters operating illegally within the protected spectrum [4]–[16]. SMAP microwave radiometer includes a digital backend that enables ground-based RFI detection and filtering. A full description of SMAP digital back end and architecture can be found in [17]. RFI detection and filtering is performed in ground processing, which allows flexibility in adjusting the algorithms post launch [18]. The RFI algorithm also provides an estimate of the RFI power level detected in each SMAP observation.

The SMAP radiometer has continuously measured Earth's thermal emissions since April 2015 within a footprint of approximately 36 × 47 km [19]. The multiyear record of RFI detected by SMAP is used to assess the RFI environment and its properties. This article reports an analysis of the RFI environment as observed by SMAP, particularly properties of the RFI sources observed that can be inferred from SMAP multiple detectors, as well as information on changes in the RFI environment over time.

The next section reviews SMAP RFI detection algorithms and their capabilities in detecting differing RFI source types. These properties are then used in Section III to obtain information on the prevalence of differing source types in the RFI environment, followed by an examination of the time evolution of the global environment in Section IV. The last section describes an RFI source reporting and monitoring software tool that has been developed to produce automatically a list of persistent RFI sources observed by SMAP on a weekly basis.

II. SMAP RFI Detection and Filtering

SMAP ground processing software implements nine distinct algorithms to detect RFI in each "footprint" measurement (representing approximately 9.6 ms of scene observation time). The algorithms use the datasets provided by SMAP digital backend for each footprint, which consist of "fullband" power and kurtosis measurements in 32 sub-intervals of time and "subband" power and kurtosis measurements for each of 16 sub-channels in eight sub-intervals of time. The latter comprises the eight

Manuscript received February 18, 2021; revised May 12, 2021; accepted June 14, 2021. Date of publication June 28, 2021; date of current version July 29, 2021. *(Corresponding author: Alexandra Bringer.)*

A. Bringer and J. T. Johnson are with the ElectroScience Laboratory, The Ohio State University, Columbus, OH 43212 USA (e-mail: bringer.1@osu.edu; johnson.1374@osu.edu).

Y. Soldo is with the European Spatial Agency, 2201 AZ, Noordwijk, The Netherlands (e-mail: yan.soldo@nasa.gov).

D. M. Le Vine and J. R. Piepmeier are with the NASA Goddard Space Flight Center, Greenbelt, MD 20771 USA (e-mail: david.m.levine@nasa.gov; jeffrey.r.piepmeier@nasa.gov).

P. Mohammed is with the NASA Goddard Space Flight Center, Greenbelt, MD 20771 USA, and also with the Morgan State University, Baltimore, MD 21251 USA (e-mail: priscilla.n.mohammed@nasa.gov).

S. Misra is with the NASA Jet Propulsion Laboratory, Pasadena, CA 91109 USA (e-mail: sidharth.misra@jpl.nasa.gov).

P. de Matthaeis is with the NASA Goddard Space Flight Center, Greenbelt, MD 20771 USA, and also with the Universities Space Research Association, Columbia, MD 21046 USA (e-mail: paolo.dematthaeis@nasa.gov).

Digital Object Identifier 10.1109/JSTARS.2021.3092996

time by 16 frequency point spectrogram from which the brightness temperature is computed. All of these measurements are provided for both horizontal and vertical polarizations and for the third and fourth Stokes parameters (excepting the kurtosis for the third and fourth Stokes measurements). A description of these products is detailed in [17].

The nine detection algorithms applied to both the H and V polarizations are

1) fullband pulse (Pulse);
2) fullband kurtosis (Kurt);
3) fullband third Stokes (T3);
4) fullband fourth Stokes (T4);
5) subband kurtosis (Kurt16);
6) subband third Stokes (T316);
7) subband fourth Stokes (T416);
8) subband cross-frequency 1.2 ms (CF1);
9) subband cross-frequency 9.6 ms (CF8).

Generally, each of the detectors, except the fullband and subband kurtosis, operates by comparing the deviation of a particular measurement T_A from its expected mean m to a threshold, with the threshold typically set as a multiple $\beta_{\mathrm{detector}}$ of the expected standard deviation of the measurement σ_{ft}, with detection declared for measurements satisfying

$$|T_A - m| \geq \beta_{\mathrm{detector}}\, \sigma_{\mathrm{ft}}. \tag{1}$$

The threshold values $\beta_{\mathrm{detector}}$ are parameters of the ground processing software for each algorithm, and could be made a function of space. Indeed, it was found post-launch that coastal transitions caused false alarms for the fullband (i.e., "time domain") and fourth Stokes detectors, so that higher detection thresholds were set on coastlines for these particular algorithms. The kurtosis algorithms operate in a similar fashion; however, they operate on the calculated moments of the measurements (second and fourth moments). The detection is declared if the kurtosis of the calculated moments deviate too much from the kurtosis value of a Gaussian distribution (i.e., 3). Each detection algorithm can flag "pixels" in the measured spectrogram; flags are combined through an "OR" operation in order to maximize the probability of detecting RFI contributions. This combined detector is referred as maximum probability of detection (MPD).

Note the application of the SMAP detection algorithms in a "two-sided" fashion, i.e., both anomalously high and low powers are flagged in order to reduce any biases caused by RFI filtering. The combined set of thresholds for the algorithms is set so that approximately 5% of spectrogram pixels are flagged in the absence of RFI (i.e., the "false alarm" case).

After detection, the filtered and unfiltered antenna temperatures are reported as an integration over the 8×16 spectrogram either excluding (filtered) or including (unfiltered) the pixels flagged as containing RFI. The difference between the unfiltered and filtered integrated quantities is labeled the "RFI level" that indicates the amplitude of the RFI contributions. When RFI impacts the entire spectrogram and thus there are no useful data left, no filtered antenna temperature and RFI level can be estimated. This situation usually occurs when strong RFI sources are observed. As a result, the portion of the high amplitude RFI sources where this happens are not included in the following analysis. Also, the loss of spectrogram data due to RFI filtering degrades SMAP radiometric resolution even with the successful reduction of some of the RFI contributions. SMAP reports for each footprint an estimate of the uncertainty that incorporates information on the number of spectrogram pixels flagged. It is also noted that the SMAP receiver saturates for strong RFI around 2500 K in vertical polarization and 2200 K in horizontal polarization. This leads to significant difference of RFI levels for the same sources whether they are observed by SMAP or SMOS, because SMOS saturates at the higher RFI levels. Therefore, the RFI levels reported by SMAP are lower than those reported by SMOS.

All subband algorithms operate on individual spectrogram "pixels" except for the CF8 algorithm, which first integrates the spectrogram over time into 16 frequency channels by a single time sample prior to cross-frequency detection. All time subsamples corresponding to a sub-channel detected by this algorithm are then flagged.

This combination of detectors was developed to provide sensitivity for sources that are localized in either time (the fullband pulse and kurtosis detectors) or frequency (both cross frequency detectors), that are not unpolarized as expected from natural surfaces (the fullband and subband third and fourth Stokes detectors), or non-Gaussian kurtosis values (fullband and subband kurtosis detectors). Although previous studies have shown that kurtosis detectors are more suitable to detect pulsed source types, they also detect more continuous sources at higher amplitude levels. General expectations are also that the cross-frequency detectors should provide the greatest sensitivity to sources localized in frequency.

III. Detector Statistics and RFI Sources Properties

Given that the sensitivities depend on source type [20] and that the behavior of SMAP RFI detectors differ depending on source types [21], some information on the prevalence of source types can be obtained through an examination of detector statistics.

As an example, Fig. 1 plots the percentage of SMAP vertically polarized footprints having a specified RFI level with any pixel flagged by individual RFI algorithms for the period 2015 to 2019. Note that this analysis includes false alarm contributions, which should exhibit a greater significance at RFI levels less than a few Kelvins. Further, the values of the percentages shown for low RFI levels are indicative of the differing false alarm rates of the individual detectors.

Even considering the differing false alarm rates of the detectors, the RFI levels at which the detection percentages increase show that the cross frequency algorithms appear to be the most effective in flagging RFI sources across all RFI levels. Specifically, these detectors flag more than 90% of the footprints having an RFI power greater than 3 K. Both the subband kurtosis and polarimetric detectors also exhibit significant sensitivity to RFI sources at low to moderate RFI levels, while the fullband polarimetric, pulse, and kurtosis detectors all show a greater percentage of flagging for RFI levels greater than approximately 5–10 K.

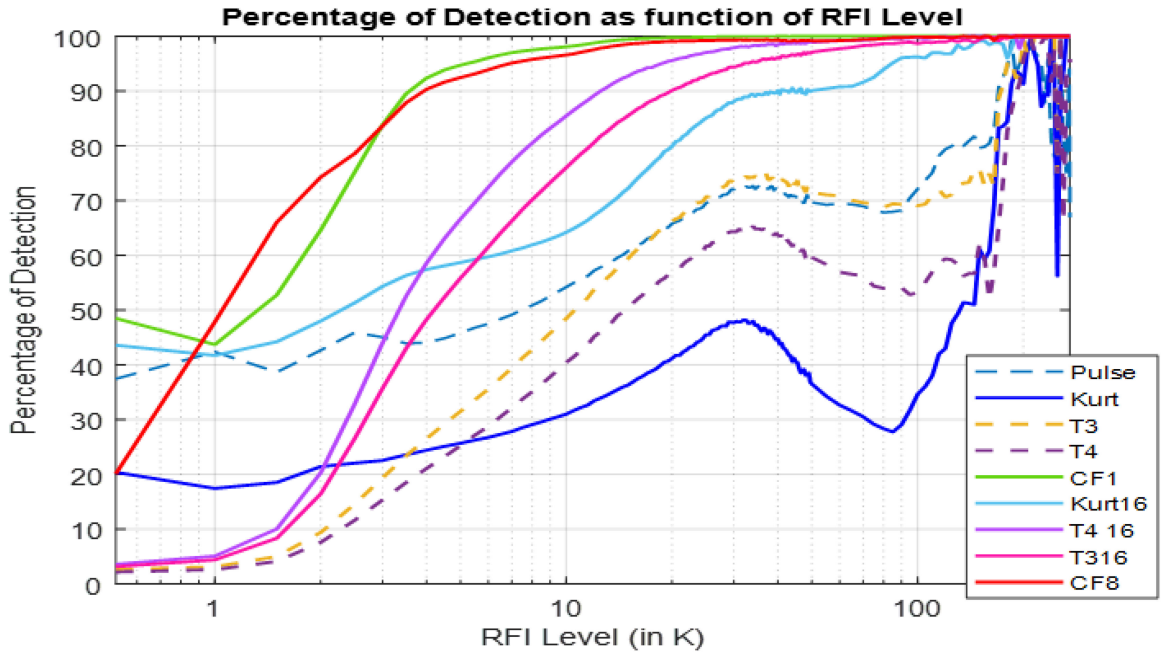

Fig. 1. Percentage of detection for each of the RFI algorithms as function of the RFI level for the five-year mission in V polarization.

Despite the use of a multi-year dataset in this analysis, the number of footprints characterized by RFI levels $>$ 100 K remains limited due to the fact that the pulse algorithm blanks all pixels for many of these footprints. In this case, the filtered antenna temperature is set to "not a number" and the RFI level cannot be estimated by simply taking the difference between the unfiltered and filtered antenna temperatures. The small number of footprints with high RFI Level in turn yields a greater degree of varying percentages observed within this range. Similar results are also observed in horizontal polarization. The dominance of the cross-frequency detectors suggest that the RFI environment contains predominately sources that are localized in frequency.

Data were also reprocessed to obtain the RFI level that would be detected if only that particular individual detector were turned on for each footprint during the period of September 2015 to June 2019. Fig. 2 displays the results of both the fullband [plot (a)] and subband [plot (b)] analysis, with the horizontal axis representing the RFI level obtained from the combination of all algorithms.

The results again show that the cross frequency detectors are responsible for most of the RFI detections; the RFI level reported in the data is near equal to the RFI reprocessed using the cross frequency detectors only, particularly for RFI levels greater than approximately 10 K. Every detector is also shown to contribute to the total. Among the fullband algorithms, the pulse detector is observed as the most active.

Given that the detector performance is a function of the source types encountered for a specified RFI level, these results again suggest the greater prevalence of the narrowband (impacted a small number of frequency channels) and continuous (impacted all the time measurements) source types in the global RFI environment across all RFI levels. It is also possible to obtain further

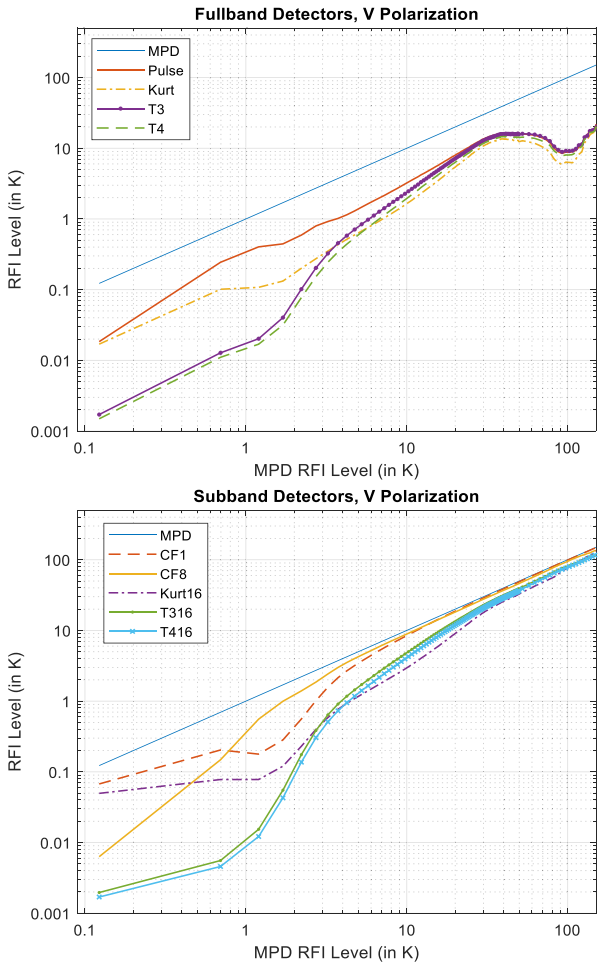

Fig. 2. RFI level reprocessed for individual detectors as function of the RFI level reported in the data for a) fullband and b) subband detectors, V Polarization.

information on the RFI environment through a classification of the sources observed in SMAP footprints into categories, for example, "narrowband pulsed," "wideband pulsed," etc. as in [22] and [23]. Therefore, continuing efforts to develop automated approaches for this process will be reported in future studies.

Ideally, the filtered antenna temperatures after SMAP RFI filtering algorithm should be free of RFI. However, an examination of the SMAP data clearly shows evidence of locations where residual RFI contributions remain even after the application of RFI detection and filtering algorithms. Sources with these "wideband" and "continuous" emissions are a particular challenge for SMAP detection algorithms and are likely a frequent contributor to non-filtered RFI, or residual RFI, which is an ongoing concern given its impact on SMAP science data. The application of SMAP data quality flags, however, can partially mitigate this residual RFI by eliminating from further processing any footprints with an excessive portion of the spectrogram removed. The SMAP mission also flags soil moisture retrievals in "urban" regions (as determined by an ancillary mask) as subject to greater uncertainty. The combination of the RFI quality flag and the urban flag eliminate a significant fraction of the apparent residual RFI from impacting science retrievals, but some fraction of corrupted data still remains. To address this issue, an algorithm that identifies spatial anomaly using a multi-footprint approach has been proposed in [24], [27]. Analyses of time variations of SMAP datasets are also under development for this purpose.

IV. Time Evolution of the Global RFI Environment as Observed by SMAP

Changes in RFI environment can be assessed considering multiple metrics (time, global, or local spatial scales). In this section, it was chosen to analyze the RFI environment on a global scale in order to analyze overall trends over time and not at a more local scale as it is done in the rest of the article. Since the RFI environment is changing from week to week or month to month, this section presents a way to assess the change in the global RFI environment in order to understand whether the impact of RFI has been constant throughout the SMAP mission or has diminished or increased over time. Indeed, Fig. 3 plots the RFI Level averaged globally and over 8 d (the SMAP revisit time) for the period May 2015 to December 2019 for horizontal and vertical polarizations. The globally averaged RFI level, which shows a mean value near 0.3 K, includes contributions from both RFI sources and false alarms. The occurrence of increase early in 2015 is from the "activation" of all RFI detectors over the entire globe, unlike in the earlier post-launch period in which all detectors were applied only over land masses.

Although relatively stable, the globally averaged RFI level shows a slight decreasing trend, with both polarizations exhibiting similar behaviors. Note also the presence of a few outliers in the time series that require further examination.

To reduce the impact of false alarms, the same quantities in Fig. 3 are plotted in Fig. 4, excluding however those footprints reported as having RFI levels < 2 K. In this case, the globally averaged RFI level is in the 6–8 K range, and is slightly higher

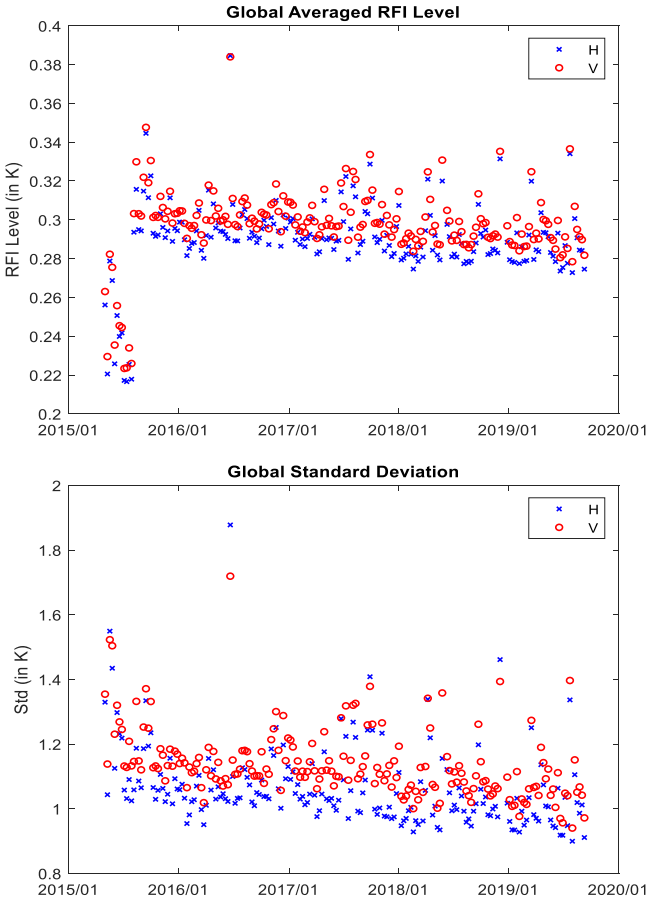

Fig. 3. Global RFI level (top) and standard deviation (bottom) in vertical (red) and horizontal (blue) polarizations averaged over 8 d, May 2015 to December 2019.

for vertical polarization. A more significant (but still small) decreasing trend is observed in this case, suggesting that either the number of RFI sources or their average amplitude diminishes in time. These results, which do confirm the occurrence of the variations in the RFI environment in time, emphasize the importance of continued monitoring of the RFI environment. Although the source of the decreasing trend is difficult to verify, the efforts of both the SMOS [26] and SMAP teams in reporting RFI sources to the national spectrum enforcement authorities have probably contributed to the decreasing trend observed. Both teams are continuing reporting activities, and the SMAP team has developed an automated software tool to support this process as described in the next section.

V. SMAP RFI Monitoring Tool and Resulting Datasets

An automatic tool has been developed as a joint effort between The Ohio State University [16] and the NASA Goddard Space Flight Center [27] to archive the RFI sources detected by the SMAP processor on a weekly basis. The list of the sources is archived in a table that provides information on the location of the sources, as well as statistics about the RFI level and frequencies (using the SMAP subbands at 1401.5 to 1425.5 MHz) impacted by the RFI sources.

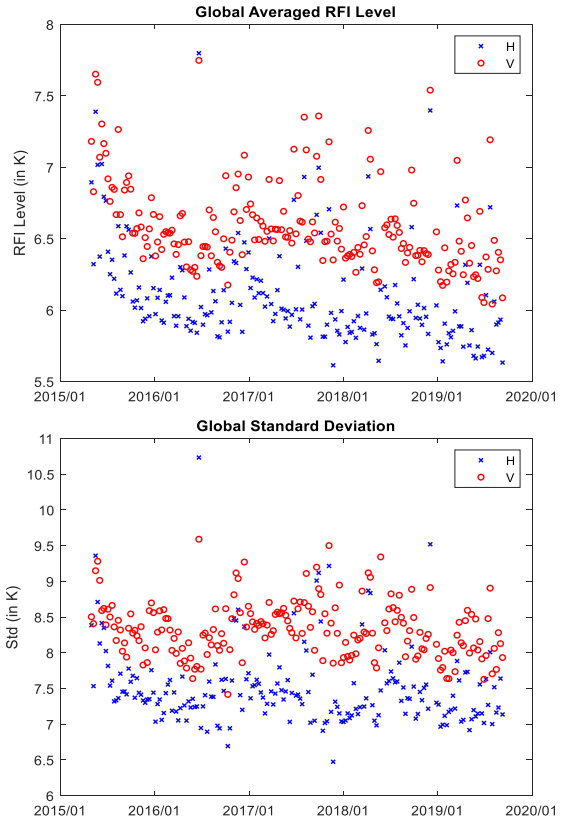

Fig. 4. Global RFI level (top) and standard deviation (bottom) in vertical (red) and horizontal (blue) polarizations averaged over 8 d for the entire SMAP mission computing using only footprints with an RFI level $>$ 2 K, May 2015 to December 2019.

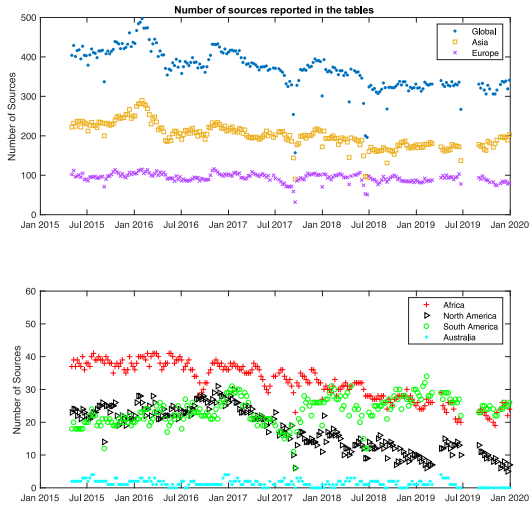

Fig. 5. Number of sources reported by SMAP RFI monitoring tool versus time globally (blue dots on the top figure) and continent by continent. (a) Asia. b) Africa, North America, South America, and Australia.

The table is the merged result of two processors. One was developed at The Ohio State University and mainly provides statistical information about the sources. The second was developed at NASA Goddard Space Flight Center in order to provide a precise location of sources as well as some information about the RFI level for both polarizations [27]. Designed to identify sources that are expected to be locatable by ground personnel to facilitate enforcement actions, the tool therefore focuses on sources that have RFI levels greater than a threshold (10 K) and are frequently detected (in at least 25% of the footprints for one month). These criteria are applied for measurements in either the horizontally and vertically polarized brightness temperatures but a source detected in both polarizations at a given location is counted only once.

Sources meeting these criteria are reported in terms of their location, RFI level, and the SMAP frequency sub-channels impacted (using the 16 SMAP frequency subbands from 1401.5 to 1425.5 MHz). Source locations are determined using the algorithm reported in [27], which has been shown to provide locations accurate to within a range of 1-8 km (despite SMAP $\sim$ 40 km footprint) through the use of SMAP measurements of a source in multiple overpasses. The algorithm also estimates the averaged RFI level in both horizontal and vertical polarizations at that location. In case of very strong sources, no filtered antenna temperature is available as the MPD flag blank all the spectrogram. Therefore, in these situations, the RFI level cannot be simply calculated from the difference between the antenna temperature before and after RFI mitigation. In that case, the algorithm uses the valid filtered antenna temperature nearby the source to compute the interpolated value at the location of the source. This provides an estimation of RFI level for the strongest sources, i.e., with RFI level $>$ 100 K.

Because weekly tables have been created for the entire SMAP mission duration, it is possible to examine temporal and spatial trends in the reported source information to obtain additional insight into the RFI environment. As an example, the upper curve in Fig. 5(a) plots the number of sources reported in the table for the period Jan 2015 to December 2019. The number of sources reported, i.e., that satisfy the criteria described previously, shows a decreasing trend with time, indicating a decrease in the number of persistent and strong sources impacting SMAP since the beginning of the mission. The number of sources also exhibits an unexpected seasonal pattern that motivates further examination.

Because the location of each source is also reported, it is possible to examine temporal trends in distinct regions. Fig. 5 includes the number of sources reported on each continent. It is perhaps not surprising that Asia has the largest number of reported sources given its geographic area, with the results also showing Asia as the primary source of the global decreasing trend, as well as the seasonal trend in RFI sources observed. The number of sources on other continents is smaller and also more stable in time as observed in Fig. 5b). One can also note a significant decrease of the number of sources in North America since January 2017. An illustration of the seasonal pattern observed in China is provided in Fig. 6.

Fig. 6 presents the persistence of the strongest RFI sources (RFI level $>$ 10 K) for winter (top row) and summer (lower row) of 2016 (first column), 2017 (second column), and 2018 (last column) in East Asia. The persistence is defined as the percentage of SMAP overpasses impacted by RFI $>$10 K. The strong sources that are visible in the Beijing area in every

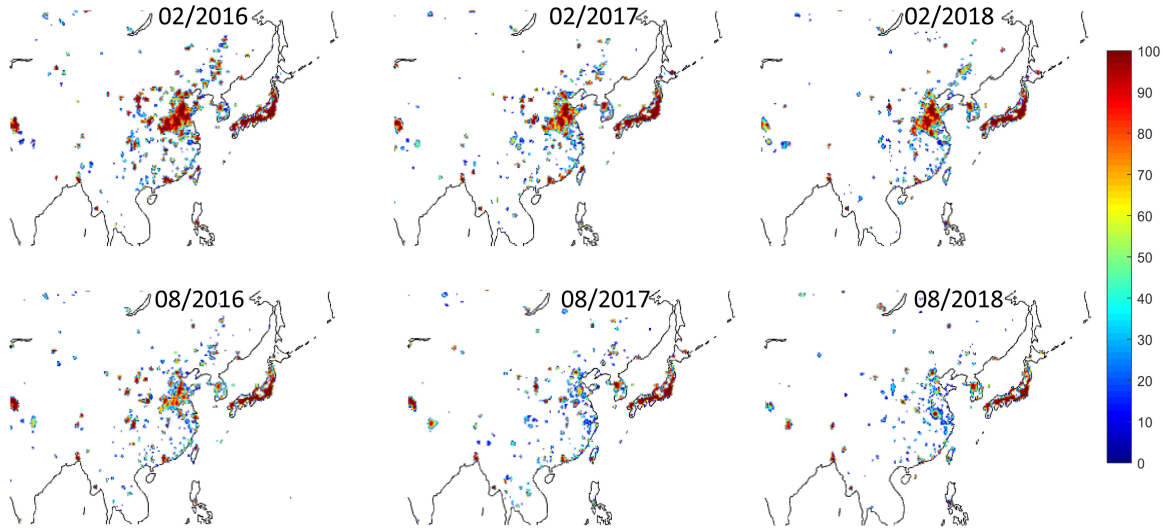

Fig. 6. Map of East Asia to illustrate the seasonal pattern of the persistence of the strongest RFI sources (RFI level >10 K) in China.

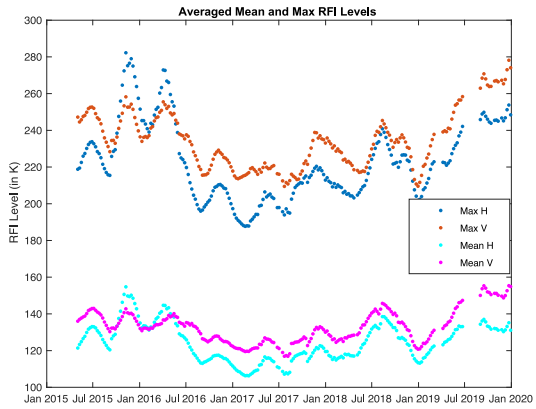

Fig. 7. Variations of the mean and max RFI levels with time averaged over the RFI table.

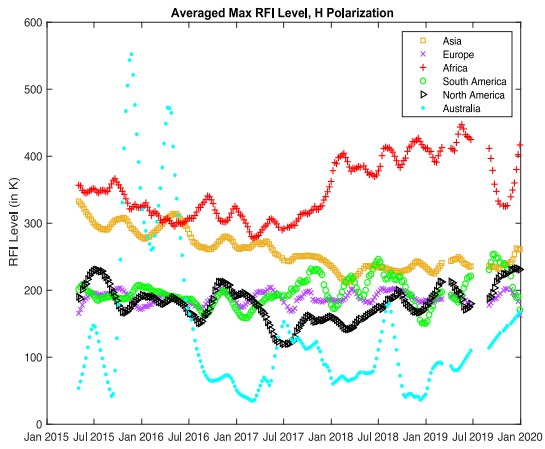

Fig. 8. Variations of the maximum RFI level in horizontal polarization continent by continent.

SMAP overpass during the winter (i.e., the persistence is close to 100%) are no longer visible in the summer as the persistence decreases significantly in summer and is close to 0 in August 2017 and August 2018. This phenomenon repeats each year and was also observed in 2019. However, the explanation for such a seasonal pattern has not been clearly identified and remains under investigation.

RFI amplitude information is also available in the tables produced both in terms of the mean RFI level observed over the four-week period and the maximum RFI level at a given location. Fig. 7 plots these quantities averaged over the entire table versus time. The trend versus time is more complex in this case, and shows a particularly variable behavior from mid-2015 to mid-2016. Fig. 8 provides insight into this behavior by again separating the global results by continent, in this case for the maximum monthly RFI level observed. Note also in Fig. 8 that Africa exhibits the highest average RFI level for nearly the entire time series, with the exception of the period mid-2015 to mid-2016 for which the anomalous global trend was observed in Fig. 7. Because the number of sources reported in Africa in Fig. 5 slightly decreases in time, the increasing RFI levels observed in Africa after mid-2017 suggest that the sources with low RFI amplitudes were turned OFF and only the strongest RFI sources are still observed.

The decrease of the maximum RFI level in Asia again indicates an improvement in the RFI environment in Asia since the number of sources also diminishes with time. South America and Europe appear more stable in time both in terms of the number of sources and their RFI levels.

The average max RFI level in North America shows a slightly decreasing trend beginning in 2017. Finally, there is an association between the anomalous behavior from mid-2015 to mid-2016 identified in the global analysis with that of source changes in Australia.

To investigate this behavior, the reported source locations were used to track specific sources and their evolution in time. A total of 21 sources were identified in Australia over the time period examined in Fig. 8, the locations of which are shown in Fig. 9. The time variation of the maximum RFI level

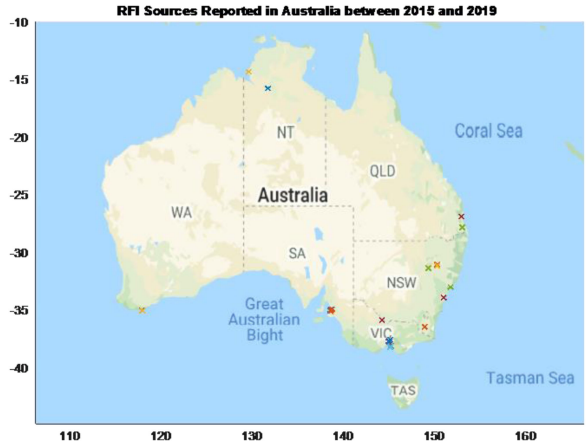

Fig. 9. Locations (indicated by "x") for all RFI sources observed in Australia, May 2015 to December 3019.

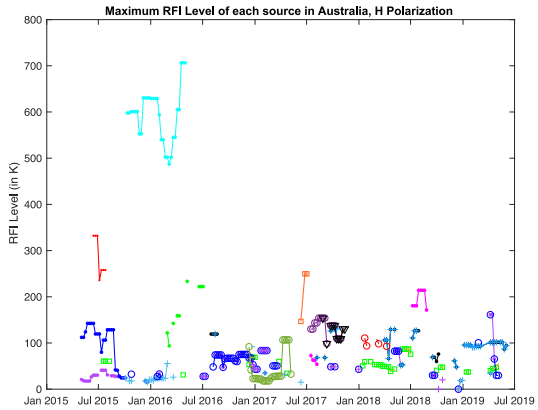

Fig. 10. Variations of the maximum RFI level for each source identified in Australia, May 2015 to December 2019.

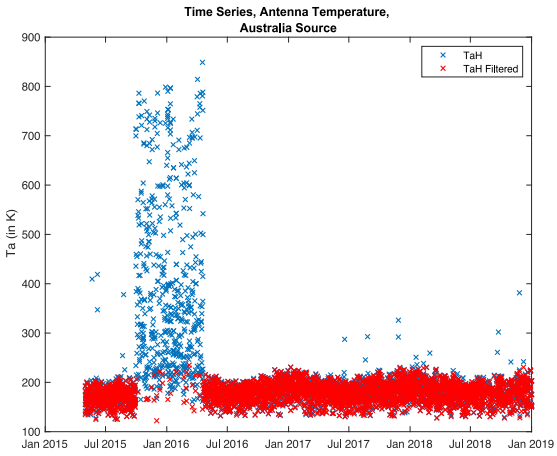

Fig. 11. Time series of the antenna temperature before (blue crosses) and after (red crosses) RFI detection and filtering for the source in Australia.

in horizontal polarization for each source (i.e., one color or symbol on the plot), is illustrated in Fig. 10. The separation of RFI levels by source shows that a single strong source was responsible for the anomalous behavior observed in Fig. 8. Moreover, this source is listed in the table only during this

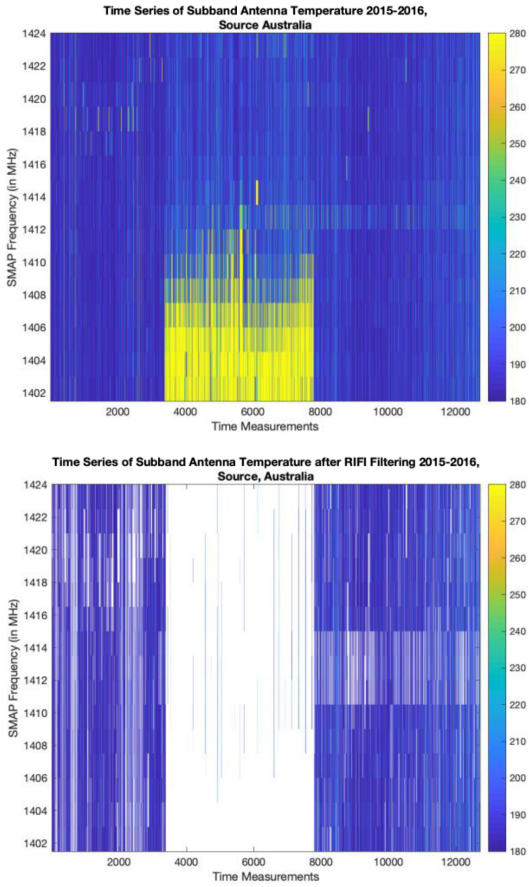

Fig. 12. Time series of the subband antenna temperature in horizontal polarization (in K) for 2015 to 2016 before (top) and after (bottom) RFI filtering.

period of time, i.e., between the summer 2015 and 2016. However, given the precise location provided by the RFI table, a detailed analysis of this source for the entire mission is still possible.

The analysis of the time series of the antenna temperature provides a better understanding of the RFI situation at that particular location. Fig. 11 presents the time series of the antenna temperature in horizontal polarization before (blue crosses) and after (red crosses) RFI detection and filtering. While this site is usually lightly impacted by RFI (filtered antenna temperatures very close to the unfiltered antenna temperatures most of the time), the measured antenna temperatures reached high values (up to 800 K) during the summer 2015 continuing into early 2016, denoting the presence of a strong RFI source emitting at that location.

The data within Fig. 12 also demonstrates that this source probably ceased emitting after that period as only occasional RFI are observed in the data after 2016. Given SMAP back-end capabilities, it is possible to estimate which frequencies were more impacted by this source. The top plot of Fig. 12 represents the time series of the subband antenna temperature in the horizontal polarization (in K) for 2015–2016 before RFI detection and filtering. Note the strong, continuous and narrowband RFI source, which appears to emit in the 1401.5 to 1409 MHz band, and which exhibits a reduced effect upon the higher frequencies.

The bottom plot of Fig. 12 represents the same time series after RFI filtering by the MPD flag. Given the strength of the RFI, all spectrograms were flagged by the pulse algorithm. The blanking of all the radiometer measurements for the entire period of source emissions results in no filtered antenna temperatures (as observed on Fig. 11) for this period. Before and after that period, pulsed RFI instances were observed with the occasional identification of some parts of the spectrograms as RFI by the MPD flag.

This example also illustrates the good performance of the different algorithms in the presence of strong and continuous narrowband sources.

VI. Conclusion

The multiyear dataset available from SMAP RFI algorithms provide extensive information on the RFI environment at L-band. Analysis of the behavior of SMAP individual RFI detectors suggests a prevalence of RFI sources that are localized in frequency across all RFI levels encountered. Analyses of trends in the global RFI level showed a slowly decreasing trend that is primarily associated with a decrease in the number of sources and their amplitudes in Asia. Although seasonal trends of RFI were also observed in Asia, the source of these trends has yet to be identified, and is a subject of continuing inquiry. Analyses of the source properties derived with the SMAP automated RFI monitoring tool again confirmed a slow decreasing trend of the strong number of sources indicating an improvement in the RFI environment. These results also emphasized the differing behaviors that are occurring in various regions of the world. The results of this article also demonstrate the occurrence of temporal variations in the RFI environment and the associated need for continuing spectrum monitoring and enforcement activities.

References

[1] Y. H. Kerr, P. Waldteufel, J. -. Wigneron, J. Martinuzzi, J. Font, and M. Berger, "Soil moisture retrieval from space: The soil moisture and ocean salinity (SMOS) mission," *IEEE Trans. Geosci. Remote Sens.*, vol. 39, no. 8, pp. 1729–1735, Aug. 2001.

[2] D. M. Le Vine, G. S. Lagerloef, F. R. Colomb, S. H. Yueh, and F. A. Pellerano, "Aquarius: An instrument to monitor sea surface salinity from space," *IEEE Trans. Geosci. Remote Sens.*, vol. 45, no. 7, pp. 2040–2050, Jul. 2007.

[3] D. Entekhabi *et al.*, "The soil moisture active passive (SMAP) mission," *Proc. IEEE*, vol. 98, no. 5, pp. 704–716, May 2010.

[4] R. Oliva *et al.*, "SMOS radio frequency interference scenario: Status and actions taken to improve the RFI environment in the 1400–1427-MHz passive band," *IEEE Trans. Geosci. Remote Sens.*, vol. 50, no. 5, pp. 1427–1439, May 2012.

[5] D. M. Le Vine, P. de Matthaeis, C. S. Ruf, and D. D. Chen, "Aquarius RFI detection and mitigation algorithm: Assessment and examples," *IEEE Trans. Geosci. Remote Sens.*, vol. 52, no. 8, pp. 4574–4584, Aug. 2014.

[6] S. Misra and C. S. Ruf, "Detection of radio-frequency interference for the Aquarius radiometer," *IEEE Trans. Geosci. Remote Sens.*, vol. 46, no. 10, pp. 3123–3128, Oct. 2008.

[7] D. M. Le Vine and P. de Matthaeis, "Aquarius active/passive RFI environment at L-band," *IEEE Geosci. Remote Sens. Lett.*, vol. 11, no. 10, pp. 1747–1751, Oct. 2014.

[8] C. Ruf, D. Chen, D. L. Vine, P. de Matthaeis, and J. Piepmeier, "Aquarius radiometer RFI detection, mitigation and impact assessment," in *Proc. IEEE Int. Geosci. Remote Sens. Symp.*, 2012, pp. 3312–3315.

[9] Y. Soldo, D. M. Le Vine, P. de Matthaeis, and P. Richaume, "L-band RFI detected by SMOS and Aquarius," *IEEE Trans. Geosci. Remote Sens.*, vol. 55, no. 7, pp. 4220–4235, Jul. 2017.

[10] E. Daganzo-Eusebio, R. Oliva, Y. H. Kerr, S. Nieto, P. Richaume, and S. M. Mecklenburg, "SMOS radiometer in the 1400–1427-MHz passive band: Impact of the RFI environment and approach to its mitigation and cancellation," *IEEE Trans. Geosci. Remote Sens.*, vol. 51, no. 10, pp. 4999–5007, Oct. 2013.

[11] M. Aksoy and J. T. Johnson, "A study of SMOS RFI over North America," *IEEE Geosci. Remote Sens. Lett.*, vol. 10, no. 3, pp. 515–519, May 2013.

[12] R. Oliva, S. Nieto, and F. Félix-Redondo, "RFI detection algorithm: Accurate geolocation of the interfering sources in SMOS images," *IEEE Trans. Geosci. Remote Sens.*, vol. 51, no. 10, pp. 4993–4998, Oct. 2013.

[13] R. Oliva *et al.*, "Status of radio frequency interference (RFI) in the 1400–1427 MHz passive band based on six years of SMOS mission," *Remote Sens. Environ.*, vol. 180, pp. 64–75, 2016.

[14] J. T. Johnson and M. Aksoy, "Studies of radio frequency interference in SMOS observations," in *Proc. IEEE Int. Geosci. Remote Sens. Symp.,* 2011, pp. 4210–4212.

[15] D. D. Chen and C. Ruf, "A novel method to estimate the RFI environment," in *Proc. IEEE Geosci. Remote Sens. Symp.*, 2014, pp. 215–218.

[16] A. Bringer *et al.*, "SMAP mission: Changes in the RFI environment," in *Proc. IEEE Int. Geosci. Remote Sens. Symp.,* 2018, pp. 3754–3757.

[17] J. R. Piepmeier *et al.*, "Radio-frequency interference mitigation for the soil moisture active passive microwave radiometer," *IEEE Trans. Geosci. Remote Sens.*, vol. 42, no. 1, pp. 761–775, Jan. 2014.

[18] P. N. Mohammed, M. Aksoy, J. R. Piepmeier, J. T. Johnson, and A. Bringer, "SMAP L-Band microwave radiometer: RFI mitigation prelaunch analysis and first year on-orbit observations," *IEEE Trans. Geosci. Remote Sens.* vol. 54, no. 10, pp. 6035–6047, Oct. 2016.

[19] J. R. Piepmeier, P. N. Mohammed, G. De Amici, E. Kim, J. Peng, and C. Ruf, "SMAP calibrated, time-ordered brightness temperatures L1B_TB data product," *NASA Goddard Space Flight Center, Revision A,* 2014.

[20] S. Misra, P. N. Mohammed, B. Guner, C. S. Ruf, J. R. Piepmeier, and J. T. Johnson, "Microwave radiometer radio-frequency interference detection algorithms: A comparative study," *IEEE Trans. Geosci. Remote Sens.*, vol. 47, no. 11, pp. 3742–3754, Nov. 2009.

[21] A. Bringer, J. T. Johnson, P. N. Mohammed, and J. R. Piepmeier, "Performance of SMAP radiometer RFI detection algorithms and analysis of residual RFI sources," in *Proc. IEEE Int. Geosci. Remote Sens. Symp.*, 2017, pp. 1243–1246.

[22] M. Aksoy and H. Rajabi, "Characteristics of radio frequency interference in the protected portion of L-band," in *Proc. IEEE Int. Geosci. Remote Sens. Symp.*, 2019, pp. 4539–4542.

[23] H. Rajabi and M. Aksoy, "Characteristics of the L-band radio frequency interference environment based on SMAP radiometer observations," *IEEE Geosci. Remote Sens. Lett.*, vol. 16, no. 11, pp. 1736–1740, Nov. 2019.

[24] Y. Soldo, D. L. Vine, and P. de Matthaeis, "Detection of residual 'Hot Spots' in RFI-filtered SMAP data," *Remote Sens.*, vol. 11, no. 24, 2019, Art. no. 2935.

[25] P. N. Mohammed, G. De Amici, J. Peng, and J. Piepmeier, "Smap RFI change detection," in *Proc. IEEE Int. Geosci. Remote Sens. Symp.,* 2019, pp. 8803–8806.

[26] E. Daganzo-Eusebio *et al.*, "SMOS RFI in the 1400-1427 MHz passive band: ESA's approach in RFI detection monitoring and reporting process," in *Proc. 32nd URSI GASS*, 2017, pp. 19–26.

[27] Y. Soldo *et al.*, "Recent advances in SMAP RFI processing," in *Proc. IEEE Int. Geosci. Remote Sens. Symp.,* 2018, pp. 313–315.

Alexandra Bringer (Member, IEEE) received the M.S. and Ph.D. degrees in physics from the Université du Sud-Toulon-Var, La Garde, France, in 2009 and 2012, respectively. Her studies were focused on physical oceanography and remote sensing.

She is currently a Research Scientist with the ElectroScience Laboratory, The Ohio State University, Columbus, OH, USA, since 2014, and has been working on microwave radiometry for cryosphere applications and on radio frequency interference detection and mitigation. Her research interests include Earth monitoring, microwave active and passive remote sensing for land, ocean, and cryosphere applications, and signal processing.

Dr. Bringer is currently a Science Team Member of the Soil Moisture Active Passive Mission, the Cyclone Global Satellite Systems (CYGNSS), and part of the Soil Moisture Group, NISAR Mission. She is also the Chair of the IEEE Columbus Chapter Joint Section AP-S/MTT and a Member of the Technical Committee, Frequency Allocations in Remote Sensing (FARS).

J. T. Johnson (Fellow, IEEE) received the bachelor of electrical engineering degree from the Georgia Institute of Technology, Atlanta, GA, USA, in 1991, and the S.M. and Ph.D. degrees from the Massachusetts Institute of Technology, Cambridge, MA, USA, in 1993 and 1996, respectively.

He is currently the Burn and Sue Lin Professor with the Department of Electrical and Computer Engineering and ElectroScience Laboratory, The Ohio State University, Columbus, OH, USA. His research interests include the areas of microwave remote sensing, propagation, and electromagnetic wave theory.

Dr. Johnson is a Member of commissions B and F of the International Union of Radio Science (URSI), and a Member of Tau Beta Pi, Eta Kappa Nu, and Phi Kappa Phi. He was recognized by the U. S. National Committee of URSI as a Booker Fellow in 2002. He was the recipient of the 1993 Best Paper Award from the IEEE Geoscience and Remote Sensing Society, was named an Office of Naval Research Young Investigator, National Science Foundation Career Awardee, and was the recipient of the PECASE Award in 1997.

Y. Soldo (Member, IEEE) received the bachelor's and master's degrees in aerospace engineering from the Politecnico di Torino, Turin, Italy, the master's degree in aerospace engineering from the Institut Superieur de l'Aeronautique et de l'Espace, Toulouse, France, and the Ph.D. degree from the University of Paul Sabatier, Toulouse, through sponsorship from the Centre National D'Etudes Spatiales (CNES), in 2013.

From 2014 to 2020, he was a Scientist with the Earth Sciences Division, NASA's Goddard Space Flight Center, Greenbelt, MD, USA. He is currently a Frequency Management and Technology Engineer with the Earth Observation Directorate of ESA, the European Space Research and Technology Center (ESTEC), Noordwijk, Netherlands. His research interests include microwave radiometry, machine learning, and radio-frequency interference detection and characterization.

D. M. Le Vine (Fellow, IEEE) received the Ph.D. degree in electrical engineering from the University of Michigan, Ann Arbor, MI, USA. His background is electrical engineering with specialization in electromagnetic theory and physics.

He does his research with the Earth Sciences Division, NASA's Goddard Space Flight Center, Greenbelt, MD, USA, where he works to develop techniques for microwave remote sensing of the environment from space. He was the Deputy Principal Investigator of the Aquarius mission. His research interests include passive remote sensing at the long wavelength end of the microwave spectrum (e.g., L-band) with applications to remote sensing of soil moisture and sea surface salinity.

Dr. Le Vine is a Member of the Geoscience and Remote Sensing Society (GRSS), Antennas and Propagation Society, the International Union of Radio Science (URSI), and the American Geophysical Union. He is currently a Member of the Ocean Salinity Science Team, which continues research on remote sensing of sea surface salinity, and also of the Science Team, NASA's Soil Moisture Active Passive (SMAP) mission and the Quality Working Group supporting ESA's Soil Moisture and Ocean Salinity (SMOS) mission. He was a Member of the GRSS AdCom. He was the recipient of the IEEE/GRSS Distinguished Achievement Award and the Golden Florin Award for his contributions to microwave radiometry.

P. N. Mohammed (Member, IEEE) received the B.S. degree from Florida Institute of Technology, Melbourne, FL, USA, in 1999, and the M.S. and Ph.D. degrees from Georgia Institute of Technology, Atlanta, GA, USA, in 2001 and 2005, respectively, all in electrical engineering.

She is currently with Goddard Earth Sciences Technology and Research (GESTAR), Universities Space Research Association, Columbia, MD, USA, and also with the Microwave Instrument Technology Branch, NASA's Goddard Space Flight Center, Greenbelt, MD, USA. Her research interests include radio frequency interference mitigation in microwave radiometers.

Dr. Mohammed is a Member of the Morgan State University Research Faculty, the Algorithm Development Team for the Soil Moisture Active Passive Radiometer, and the Technical Committee for Frequency Allocations in Remote Sensing (FARS).

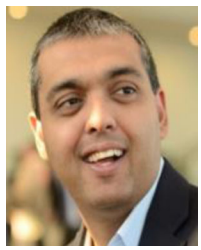

S. Misra (Senior Member, IEEE) received the B.E. degree in electronics and communication engineering from Gujarat University, Ahmedabad, India, in 2004, the M.S. degree in electrical engineering and computer science from the University of Michigan, Ann Arbor, MI, USA, in 2006, and the Ph.D. degree from the Department of Atmospheric, Oceanic and Space Sciences, University of Michigan, in 2011.

He is currently a Technologist with the NASA Jet Propulsion Laboratory (JPL), Pasadena, CA, USA. He joined JPL in 2011 as a Member of the Microwave Systems Technology Group. He was on the calibration team of the Aquarius radiometer, and was the Instrument-Scientist on the RACE mission. He was also the Digital Back-End Lead for the CubeRRT mission. He is currently on the Science Team of SMAP, as well as Ocean Vector Winds for the COWVR mission, and Radiometer Calibration Team Member for the Juno microwave radiometer. He is also the Instrument Manager for the PALS airborne system. His research interests include radio frequency interference algorithm development and mitigation, microwave radiometer system development, and calibration.

Dr. Misra is the current Chair Vice for the IEEE Geoscience and Remote Sensing Society (GRSS) and an Associate Editor for the GeoScience and Remote Sensing Letters.

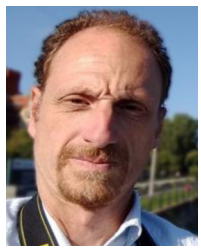

P. de Matthaeis (Senior Member, IEEE) received the laurea degree (summa cum laude) in electrical engineering from the University of Rome "Tor Vergata", Rome, Italy, and the doctor of science degree in electrical engineering from The George Washington University, Washington, DC, USA.

After graduation, he was with ESTEC, European Space Agency, Noordwijk, The Netherlands under the Young Graduate Trainee program, and with the Remote Sensing Laboratory with the University of Rome "Tor Vergata." He was then with the NASA Goddard Space Flight Center, Greenbelt, MD, USA, as a Research Associate, where he is currently a Research Scientist. He was part of the Science Algorithms Calibration/Validation Team for the Aquarius instrument, and is now part of the team working on sea surface salinity estimation using SMAP. His research interests include active and passive microwave remote sensing, with a focus on electromagnetic modeling of vegetation, land and sea surface, and detection and mitigation of radio frequency interference (RFI).

Dr. de Matthaeis is a Member of the U.S. National Committee (USNC) for URSI. He was a Co-chair of the IEEE GRSS Frequency Allocations in Remote Sensing Technical Committee (FARS-TC) from 2013 to 2017, and has been its Chair since July 2017.